Volume 1 | Number 1 | Jan 2013 | Pages 1–100

Nanoscale

www.rsc.org/nanoscale

ROYAL SOCIETY OF CHEMISTRY

This is an *Accepted Manuscript*, which has been through the Royal Society of Chemistry peer review process and has been accepted for publication.

Accepted Manuscripts are published online shortly after acceptance, before technical editing, formatting and proof reading. Using this free service, authors can make their results available to the community, in citable form, before we publish the edited article. We will replace this *Accepted Manuscript* with the edited and formatted *Advance Article* as soon as it is available.

You can find more information about *Accepted Manuscripts* in the **Information for Authors**.

ROYAL SOCIETY OF CHEMISTRY

www.rsc.org/nanoscale

ARTICLE TYPE

On-demand shape and size purification of nanoparticle based on surface area

Renming Liu, ‡ [a] Jian-Hua Zhou, ‡ [b] Zhang-Kai Zhou,*[a] Xueqin Jiang, [b] Jiaming Liu,[a] Guanghui Liu, [a] Xue-Hua Wang*[a]

In order to overcome the serious deficiency of the traditional aquatic centrifugation method in on-demand purification of metal nanoparticles, we have theoretically and experimentally developed a simple purification method based on the nanoparticles' surface area discrepancy, which can separate particles [10] with same mass but different shapes. As an example, we apply this method to obtain on-demand homogenous Au triangular nanoplates, and tune the plasmon modes of Au nanoplates into resonance with the emission of quantum dots for achieving fluorescence resonance energy transfer (FRET) between them. Moreover, due to the high homogeneity, the purified Au triangular nanoplates exhibit an excellent sensitivity to refractive index as high as 963 nm/RIU (approaching the theoretical value of 982 nm/RIU), [15] which leads to the high gauging accuracy up to 80 ppb and 1.0 U for sensing the bovine serum albumin and DNA polymerase in solution, respectively. Our work introduces a facile, effective strategy for separation of nanoparticles, which could achieve building blocks with scalable uniform nanosize, providing a path to precise control of metal nanoparticle's plasmon modes and efficient fabrication of nanodevices.

[20] 1 Introduction

Owing to the collective oscillations of electron gases near surfaces and interfaces (so-called surface plasmons), metallic plasmonic nanomaterials exhibit remarkable instinctive advantages in manipulating electromagnetic field on nanoscale, [25] which leads to a large number of fabulous achievements in nanoscience, such as the nanofucusing, sub-wavelength optical communication, and surface plasmon enhanced spectroscopy.[1-7]

The plasmonic materials participating interactions are fundamentally dominated by plasmon modes, which correspond [30] to the oscillation form of electron gas. For example, the strong light absorption of metal nanoparticle (NP) mainly results from localized plasmon modes,[8] and the Fano resonance is caused by the interference of bright and dark plasmon modes.[9-11] So, precise

[35] *[a] State Key Laboratory of Optoelectronic Materials and Technologies, School of Physics and Engineering, Sun Yat-sen University, Guangzhou 510275, People's Republic of China. E-mail: zhouzhk@mail.sysu.edu.cn and wangxueh@mail.sysu.edu.cn.*
[b] Key Laboratory of Sensing Technology and Biomedical Instruments of [40] *Guangdong Province, School of Engineering, Sun Yat-sen University, Guangzhou 510275, People's Republic of China*
† Electronic Supplementary Information (ESI) available: The original experimental and simulation data of Au triangular nanoplate in RIS measurement, AFM data of Au triangular nanoplate, and detailed [45] *experiment demonstrations of purification processes as well as expression of theoretical considerations about the surface area-based purification method. See DOI: 10.1039/b000000x/*
‡ These authors contributed equally.

[50] control of plasmon mode can manipulate the interaction between light and matter, which can give rise to greatly expanding of basic understanding in fundamental science and efficiently building of artificial devices with fantastical functions.[12-19] Since the plasmon modes are dependent on the morphology of nanostructures,[20] the [55] heart of achieving uniform and desired plamon modes lies at the obtaining of uniform nanostructures with on-demand shape and size. On the contrary, the polydispersive nanostructures with different shapes and sizes present chaotic and hybrid plasmon modes, which obviate a variety of measurements, confound data [60] analysis, and preclude potential applications.[21-23]

Many physical methods such as photon lithography, electron-beam lithography, and ion beam lithography are employed to create a large variety of uniform nanoscale geometries and patterns, due to their high resolutions and stability; but these [65] techniques always involve complex fabrication processes, with the problems of low throughput, high cost and bad crystallization.[24,25] On the other side, chemical synthesis can facilely produce a vast number of nanostructures with high reproducibility and single crystallization,[26-30] but it is still [70] suffering from the presence of impurity, even with significant research efforts directing to optimize the synthesis conditions. Therefore, tremendous efforts were devoted into purifying the chemically synthesized materials in order to achieve nanostructures with maximum homogeneity in stead.[31-35]

[75] Despite the great achievements in chemical purifications, a disappointed situation is that some as-prepared nanoparitcles and

undesired components are always with the same mass and volume, which makes traditional aquatic centrifugation methods (usually based on the difference of material's mass, volume or density) fail to separate them. For example, Au triangular nanoplates (TNPs), who exhibit numerous outstanding characteristics and widely applications in biochemical sensor, nanowaveguide, in vivo infrared imaging, etc.,[36-39] still suffer roughly from the big obstacle of impurity.[40,41] Few effective separation methods exist for addressing this challenge (this problem not only lies in the separation of Au TNPs).[42-45]

Herein, in order to develop a facile method for obtaining uniform nanostructure, we systemically investigated the role of surface area in determining nanoparticles' dispersion ability in the solution, and then proposed a simple and effective method based on the nanoparticles' surface area discrepancy to separate uniform nanostructure from mixtures of nanoparticles with almost equal mass and volume. As a vivid example to demonstrate the advantages of our purification method, we used this method to separate on-demand uniform Au TNPs from Au SNPs with almost the same mass, and investigated the Au TNP's characteristics and useful applications stemmed from their high homogeneity. With a purity of 98%, the Au TNPs exhibit a maximum refractive index sensitivity (RIS) of 963 nm/RIU, which closed to the limit of theoretical calculation. After utilizing the highly sensitive Au TNPs to monitor the concentrations of DNA polymerase and bovine serum albumin (BSA) in solution, we found the measured detection limits are up to 1.0 U and 80 ppb, respectively. Furthermore, by selecting Au TNPs with on-demand size, we precisely tuned the plasmon modes of Au nanoplates into resonance with the emission of quantum dots, realizing the fluorescence resonance energy transfer. These results indicate great potentials of the purified Au TNPs in highly sensitive bio-sensing, imaging and nanodevice fabrication. Distinguished from many traditional purification methods which are usually based on mass, volume or density, our proposed method puts research emphasis on the instinct merit of surface area, which is very important for the material applications from solar cell to catalyst, but receives relatively few attentions in the field of purification. Our findings not only introduce a facile, effective strategy to achieve nanomaterial with high homogeneity and outstanding properties, but also expand our understanding of nanoparticle's sedimentation performance in solution, and build up a novel purification concept for nanoscience.

2 Results and discussion

2.1 Principle of surface area-based purification strategy

Au NPs synthesized using the seed-mediated method are protected by a positive-charge cetyltrimethylammonium bromide (CTAB) bilayer. Strongly electrostatic repulsion between Au NPs and the intensive Brownian motions make them stably stay in the colloidal solution with good dispersion ability. On the contrary, the attractive depletion forces arise from the presence of CTAB micelles leads to the formation of robust crystals with interparticle spacings,[46] which facilities the deposition of Au NPs. Therefore, electrostatic repulsion and attractive depletion force, as well as the Brownian motion are three main factors which determine the dispersion ability of nanoparticles in CTAB solution.

Relationships between the particle's surface area and the three aforementioned factors, *i.e.* electrostatic repulsion force ($F_{c,i}$), depletion force (F_{dep}) and Brownian vector (v_N), are expressed by the following three equations:[46,47]

$$F_{c,i} = k\sigma^2 S_i \sum_j (S_j^{TNP} + S_j^{SNP}), k = \frac{1}{4\pi\varepsilon r_{i,j}^2} \quad (1)$$

$$F_{dep} = \frac{1}{2}|\Delta\prod(t_{TNP,eff} + d_{CTAB,eff} - 1)| \cdot S^{TNP} \quad (2)$$

$$v_N^{TNP} = k_1 \cdot (S^{TNP})^{-\frac{3}{4}}, \ v_N^{SNP} = k_2 \cdot (S^{SNP})^{-\frac{3}{4}} \quad (3)$$

where $F_{c,i}$ is the total sum of the magnitude for electrostatic repulsion force which the particle i applied from its adjacent positive charged NP (j) , σ is the surface charge density (we consider σ is identical for all NPs, and the reason can be found in Fig. S1), S_i is the surface area of the NP i (TNPs or SNPs) , S^{TNP} and S^{SNP} are surface areas of the TNPs and SNPs, $r_{i,j}$ is the distance between two NPs; F_{dep} is depletion forces, $\Delta\prod$ is the osmotic pressure difference, $t_{TNP,\ eff}$ and $d_{CTAB,eff}$ are effective sizes of the NPs and CTAB micelles, d is the center-to-center interparticle spacing between two adjacent nanoplates; v_N is the root-mean-square velocity of a Brownian particle, k_1 and k_2 are constants (detailed deduction of these equations can be found in the Supporting information).
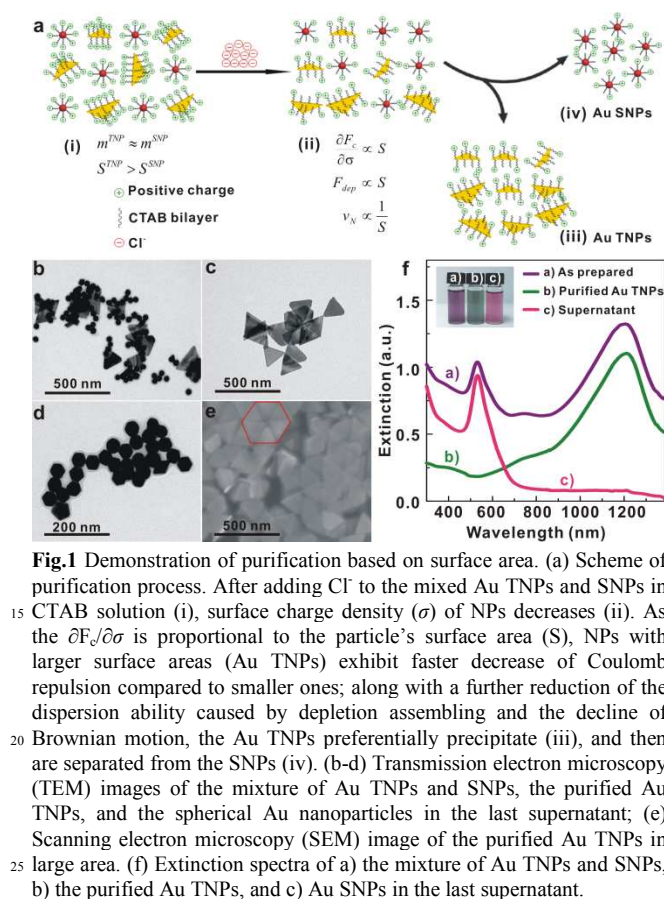
From Eq. 1, one can deduce that the $\partial F_{c,i}/\partial\sigma$ is proportional to the particle's surface area S. Thus, NPs with larger surface areas exhibit faster decrease of Coulomb repulsion as it applied with the decrease of σ. Sequentially, Eq. 2 help us understand NP with larger S shows stronger depletion force, indicating that the NPs with larger S will preferentially assemble into a collective crystals (illustrated by Fig. S1 from Supporting information). In addition, it is obviously to tell that the intensity of Brownian movement is inversely proportional to S according to Eq. 3. From the theoretical discussion above, the values of electrostatic repulsion and depletion force, as well as intensity of Brownian movement, are all dependent strongly on the nanoparticle's surface area, which could be used as an important character for the purification of nanoparticles with difference shapes and sizes.

2.2 Demonstration of surface area-based purification strategy

2.2.1 Shape purification

The steps of our particle separation method based on surface area are shown in Fig. 1a. As the prepared Au nanostructures are overcoated with CTAB bilayer, resulting in positive charges on the surfaces; the addition of Cl⁻ neutralizes part of the surface charges (see Zeta potential measurement shown in Fig. S1) and decreases the electrostatic repulsion of the nanostructures applied in solution. Since the $\partial F_c/\partial\sigma$ is in direct proportion to S (deduced by Eq. 1), the nanostructure with larger S exhibits a faster decrease of Coulomb repulsion and larger aquatic dispersion ability loss compared with the smaller ones. Meanwhile, according to Eq. 2, the nanostructures with larger S feel stronger depletion attractions and preferentially assemble into collective crystals in solution due to CTAB micelles. Moreover, with the

help of weaker Brownian motion, the nanostructure with larger S would precipitate faster than the smaller ones. So the sedimentation strategy can be summarized into 3 steps: 1) Coulomb repulsion decrease leads to dispersion ability loss; 2) depletion force induces nanostructure assembling; 3) the decline of Brownian movement intensity accelerates sedimentation. Since these three processes are all connected with nanoparticle's surface area, we could obtain purified nanostructures with on-demand shapes and sizes in sequence due to their surface area difference (detailed experiment can be found in the **Experimental methods** section and Supporting information part).
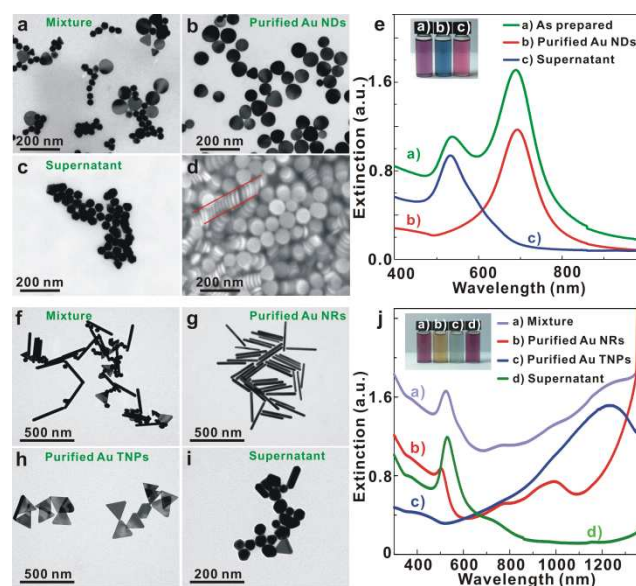

Fig.1 Demonstration of purification based on surface area. (a) Scheme of purification process. After adding Cl⁻ to the mixed Au TNPs and SNPs in CTAB solution (i), surface charge density (σ) of NPs decreases (ii). As the $\partial F_c/\partial\sigma$ is proportional to the particle's surface area (S), NPs with larger surface areas (Au TNPs) exhibit faster decrease of Coulomb repulsion compared to smaller ones; along with a further reduction of the dispersion ability caused by depletion assembling and the decline of Brownian motion, the Au TNPs preferentially precipitate (iii), and then are separated from the SNPs (iv). (b-d) Transmission electron microscopy (TEM) images of the mixture of Au TNPs and SNPs, the purified Au TNPs, and the spherical Au nanoparticles in the last supernatant; (e) Scanning electron microscopy (SEM) image of the purified Au TNPs in large area. (f) Extinction spectra of a) the mixture of Au TNPs and SNPs, b) the purified Au TNPs, and c) Au SNPs in the last supernatant.

The separation results are presented in Fig. 1b-f. Fig. 1b illustrates that the as-prepared solution contains Au TNPs with an edge length (l) distribution from 95 to 220 nm and a thickness (t) of ~7 nm (Fig. S2 in Supporting information). We count 300 TNPs and found that 42% TNPs have almost the same mass with the co-existing SNPs, with a weight discrepancy less than 10% (the estimated diameter of Au SNPs is 45 nm); this similarity in mass makes the traditional aquatic centrifugation method unable to separate these two structures. Fortunately, the surface area ratio of Au TNPs to Au SNPs with equal mass is up to 2.6, which facilitates us to separate Au TNPs from Au SNPs by the surface area difference (shown in Fig. 1c and 1d). The purification results are also demonstrated by the extinction spectra (Fig. 1f). From the extinction spectrum of the as-prepared solution (purple line), two obvious peaks are found at 535 and 1230 nm, which respectively result from the surface plasmon resonances (SPRs) of Au SNPs and Au TNPs. Comparing with the existence of only

one peak in the extinction curves of the purified Au TNPs and supernatant solution (red and green lines), the spectra indicate a high purity of the Au SNPs and Au TNPs.

In order to present the general applicability of the surface area-based purification technique, we also apply this method to separate other gold nanostructures including nanodiscs (NDs) and nanorods (NRs), and the results are presented in Fig. 2. By measuring the size of Au NDs (diameter of ~76 nm, and thickness of ~10 nm), it can be found that ~70% of Au NDs have nearly the same mass with SNPs (mass discrepancy is less than 5%), while the surface area of Au NDs is 80% larger than SNPs. This fact makes it is impossible to separate them by traditional aquatic centrifugation methods, but it is easy to obtain Au nanodiscs with a purity of over 95% using the surface area-based purification method (see Fig. 2d).

Moreover, this method is also capable to separate a mixture with three different shaped components. By employing our method, we can obtain purified Au NRs, TNPs and SNPs in sequence from the mixture (Fig. 2g-j). The results indicate that the separation of multiple nanostructures from its mixture can be successfully achieved, which provides a potential alternative strategy to obtain massive homogeneous nanostructures from the complex products prepared by solution-phase nanosynthesis.

Fig.2 Demonstration of the general applicability of the surface area-based purification method. (a-c) TEM images of a) the mixed Au NDs and b) Au SNPs, c) the purified Au NDs, and the spherical Au nanoparticles found in the last supernatant; (d) SEM image of the purified Au NDs in large area. (e) Extinction spectra of the mixture of Au NDs and Au SNPs, the purified Au NDs, and Au SNPs found in the last supernatant (Fig. 2a-d). (f-i) TEM graphs of the mixing solution, the purified Au NRs, the purified Au TNPs and the NPs in supernatant, respectively. (j) The corresponding extinction spectra of the NPs shown in Fig. 2f-i.

2.2.2 Size purification

After the demonstration of nanoparticle's separation with different shapes, we turn to utilizing this method to prepare homogenous nanoparticle with on-demand size. Since Au TNPs exhibit many fabulous properties, we take Au TNPs as an example here, as well as the following parts. By optimizing the growth conditions and our proposed "step separation" (the details can be found in **Experimental methods**) based on particle's

surface area, purified Au TNPs with edge length (l) of about 180, 160, 130, 110, 90, 70, 40 nm are acquired. The SEM images are shown in Fig. 3a-d, and Fig. S2a-c in Supporting information, respectively. Image analysis of approximately 500 particles
5 reveals that the purity of Au TNPs can easily exceed 90% and reach as high as 98% (Fig. 3a).

Fig. 3e shows the corresponding normalized extinction spectra of the purified Au TNPs, which can further demonstrate the advantage of our purification method. Counting the full width at
10 half maximum (FWHM) of the extinction spectra, one can note that the FWHM of Au TNPs (l = 160 nm) is about 166 nm, which is ~100 nm narrower than that of the unpurified Au TNPs solution (shown in Fig. S2d in Supporting information).
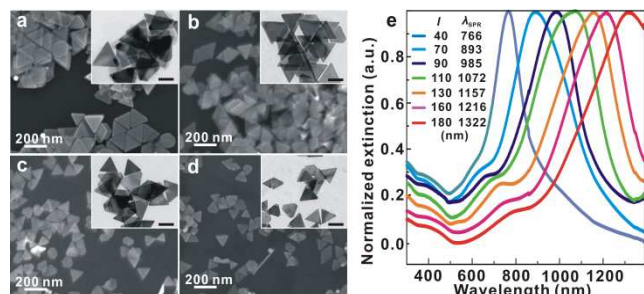
15 **Fig.3** Morphology and extinction spectra of the purified Au TNPs with different edge lengths. (a-d) SEM images of the purified Au TNPs with the average edge length of (a) 180, (b) 160, (c) 130, and (d) 110 nm, respectively. (e) Normalized UV-vis-NIR extinction spectra of the purified Au TNPs with the average edge lengths of 40, 70, 90, 110, 130,
20 160, and 180 nm. The absence of a peak around 535 nm which belongs to SPRs of Au SNPs, implies that the nanoplates are spectroscopically pure without Au SNPs. The scale bars in the insets are 100 nm.

In addition, it can be found that the SPRs mode locations (λ_{SPR}) of Au TNPs range from 766 to 1322 nm, which is the significant
25 near infrared (NIR) region (the so-called "NIR optical window") for bio-sensing; the photons within this region can provide a deeper tissue penetration and higher imaging signal-to-noise ratio.[48,49] This property of SPRs makes the uniform Au TNPs can be a powerful candidate for the design of functional bio-sensing
30 nanodevices.

It is worth mentioning that the purified nanomaterials with same shape and uniform size can be regarded as basic building blocks for the fabrication of functional nanostructures, which can provide facilities to device design[50,51] or novel pathways for the
35 investigation of fundamental rules in nanoscience. For example, if the collective structures formed by Au TNPs and Au NDs shown in Fig. 1e and Fig. 2d (marked by red line) can be controlled, they may greatly help to realize strong photon-exciton coupling which is essential for quantum communication[52,53] or
40 the study of enhanced spectroscopy.[54,55] The strong photon-exciton coupling mainly results from the immense electromagnetic field enhancements induced by the SPRs mode coupling of adjacent NPs with extreme near distance,[11,56] and the high homogeneity of build block guarantees that SPRs of
45 adjacent NPs can match with each other.

2.3 Application of the surface area-based purification method

2.3.1 Tuning the plasmon mode of nanoparticle into resonance with quantum dots
The above results prove that the surface area-based purification

50 method is a simple and effective way to obtain nanostructures with on-demand shapes and sizes, which can give rise to various important applications. Thus, we subsequently come to present some of them, and firstly we try to demonstrate the plasmon mode precise controlling of the Au TNPs *via* the surface area-
55 based purification. After selecting on-demand sizes, we achieve Au TNPs with λ_{SPR} = 782, 805, 855, and 1060 nm so as to tune the plasmon modes of Au TNPs into resonance with the NIR emission of semiconductor quantum dots (SQDs), which are generally regarded as fluorescence probes in bioassays. The
60 SQDs functioned with negatively charged carboxyl groups are purchased from Invitrogen Corporation (Qdot@ 800 ITK, Q21371MP) and the emission peak locates at 783 nm (Fig. 4a). Since the Au TNPs are overcoated with the positively charged CTAB bilayers and the SQDs are negative charged, the Coulomb
65 force would facilitate the connection of these two materials (as shown in the insert of Fig. 3b). Fig. 4a shows the emission spectra of SQDs before and after connected to Au TNPs with different plasmon modes. As the plasmon modes of Au TNPs (λ_{SPR} = 805, 855, and 1060 nm) are far from the emission band of
70 SQDs, the fluorescence intensity of SQDs only decrease about 20~30%. On the other side, the emission intensity of SQDs declines by 71% (Fig. 3b) in the mixture of SQDs and Au TNPs with λ_{SPR} = 782 nm (only 1 nm discrepancy with the emission wavelength of SQDs), showing an obvious emission quenching.
75 The dramatic emission quenching stems from fluorescence resonance energy transfer (FRET) between the SQDs and Au TNPs, in which SQDs serve as energy donors and the Au TNPs play the role of acceptors due to their exceptional energy quenching ability. Since the FRET phenomenon has been
80 successfully demonstrated for the purpose of biomedical applications and electronic devices,[57,58] precisely tuning the plasmon mode of metallic nanostructure into resonance with donor's emission energy will greatly improve the efficiency of FRET, leading to various useful applications in the design of high
85 efficient nanodevices.
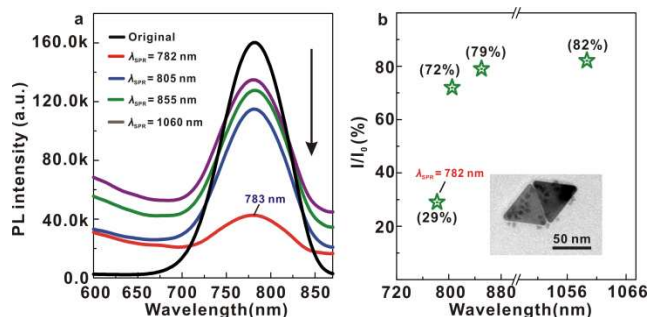
Fig.4 Fluorescence resonance energy transfer (TRET) between the SQDs and Au TNPs. (a) Photoluminescence spectra of SQDs solution without, and with the same amount of purified Au TNPs (λ_{SPR} = 782, 805, 855, and
90 1060 nm). (b) The photoluminescence intensity ratios of SQDs with the same amount of purified Au TNPs (λ_{SPR} = 782, 805, 855, and 1060 nm) to that of SQDs without Au TNPs. Insert: TEM image of SQDs attached on the surface of the Au TNPs.

2.3.2 Achieving material with maximum detection sensitivity
95 **and proteins sensing**
Sencondly, as some critical characteristics of nanomaterial are closely linked to the material's homogeneity, we turn to use our proposed method to acquire Au TNPs with maximum RIS value,

and the results of which are presented in Fig. 5. Fig. 5a and b respectively shows the experimental and theoretical normalized extinction spectra of Au TNPs with λ_{SPR} = 1258 nm in varying refractive index condition. The refractive index is adjusted by water-glycerol mixtures of different volume ratios, and the refractive index of the liquid mixture is calculated according to the Lorentz-Lorenz equation.[19]

Spectra analysis shows that the experimental RIS of Au TNPs with λ_{SPR} = 1258 nm reaches as high as 963 nm/RIU, which approaches the theoretical result of 982 nm/RIU simulated by COMSOL (Fig. 5c and d). To the best of our knowledge, this RIS value is probably the highest value in the hitherto reports of water-soluble metallic nanoparticles. We also perform the RIS experiments using the Au TNPs with λ_{SPR} = 1065 and 1191 nm (spectra results are shown in Fig. S5 in Supporting information), and their experiment RIS values also meet the simulation limits. Since it is generally confirmed that the impurity of nanostructure broaden the extinction spectra and decrease RIS, the high experimental values in RIS can be attributed to the well homogeneity of the purified Au TNPs.[59] In addition, the outstanding performance of Au TNPs in RIS measurement can also be ascribed to their very thin thickness (~7 nm) and sharp tips, which induces an extremely plasmonic enhanced electromagnetic filed.[60]
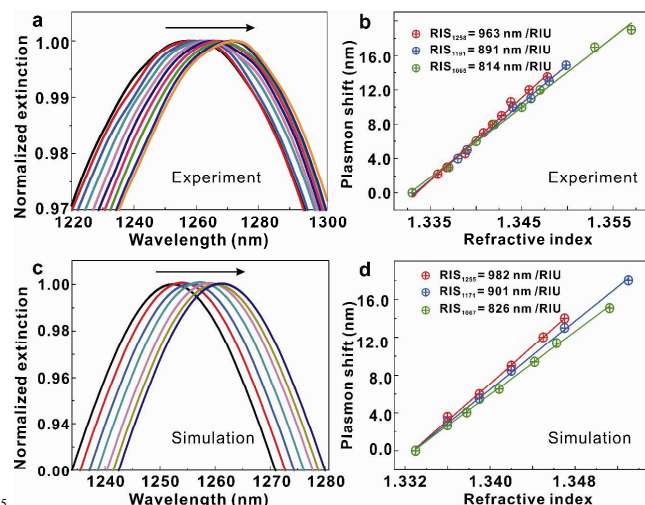
Fig.5 Refractive index sensitivity of the purified Au TNPs. (a) Experimental and (c) theoretical extinction spectra of Au TNPs (λ_{SPR} = 1258 nm) in water-glycerol liquid mixtures of varying compositions. Each spectrum is normalized to its maximal extinction intensity. The arrows indicate the direction of increasing volume percentage of glycerol. (b) Experimental dependence of the longitudinal plasmon shift on the refractive index of the liquid mixture for the Au TNPs with the SPR locations at 1258 (red circles), 1191 (blue circles), and 1065 nm (green circles). (d) Theoretical dependence of the longitudinal plasmon shift on the refractive index of the liquid mixture for the Au TNPs with the SPR locations at 1255 (red circles), 1171 (blue circles), and 1067 nm (green circles). The lines are linear fits.

Following the RIS measurement, we choose the Au TNPs with maximum RIS value, and apply this uniform, highly sensitive Au TNPs as a bio-sensing element to monitor the concentrations of BSA and DNA polymerase in solution. BSA is often used as a protein concentration standard in lab experiments. It has numerous biochemical applications including enzyme-linked immunosorbent assay, immunoblots, and

immunohistochemistry.[61] DNA polymerase is an enzyme that creates DNA molecules by assembling nucleotides, the building blocks of DNA. It is required to help duplicate the cell's DNA when a cell divides in vivo and also play an important part in polymerase chain reaction (PCR) in vitro.[62] So, we employed the purified Au TNPs with λ_{SPR} = 1217 and 1192 nm to detect the BSA and DNA polymerase, respectively. The normalized extinction spectra of Au TNPs in BSA and DNA polymerase solution with different concentration are presented in Fig. 6a and c, and the corresponding spectra analysis results are shown in Fig. 6b and d. From the fitting results, one can see that the shifts of plasmon peak increase linearly to the concentrations of proteins, with the concentration sensitivities (CRs) of BSA and DNA polymerase being 18.4 nm/ppm and 0.69 nm/U, and their detection limits are up to 80 ppb and 1.0 U, respectively.
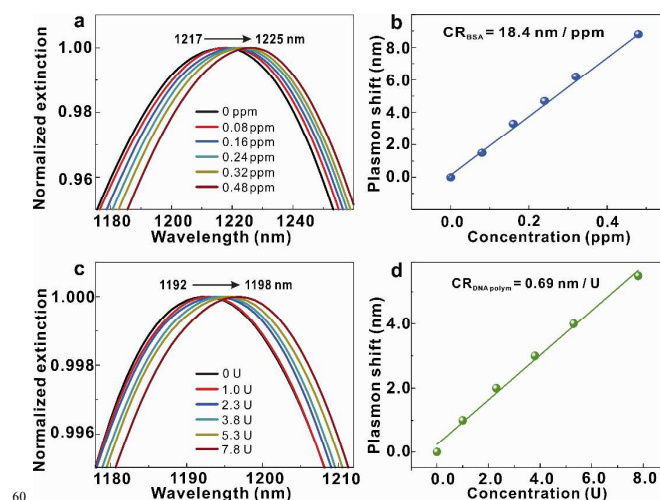
Fig.6 BSA and DNA polymerase detections by the purified Au TNPs. (a, c) Extinction spectra of the purified Au TNPs (λ_{SPR} = 1217 and 1192 nm) in water-BSA (a) and water-DNA polymerase (c) mixtures of varying concentrations, respectively. Each spectrum is normalized to its maximal extinction intensity. The arrows indicate the direction of increasing concentrations of proteins. (b, d) Dependence of the longitudinal plasmon shift on protein concentrations of BSA (b) and DNA polymerase (d) in the liquid mixtures based on Au TNPs with the SPR locations at 1217 (blue spheres) and 1192 (green spheres), respectively. The lines are linear fits.

3 Experimental methods

3.1 Materials

Gold (III) chloride trihydrate (HAuCl$_4$·3H$_2$O, > 99%), sodium borohydride (NaBH$_4$, 99%), L-ascorbic acid (C$_6$H$_8$O$_6$, > 99%), cetyltrimethylammonium bromide (CTAB, 99%), sodium citrate (C$_6$H$_5$O$_7$Na$_3$·2H$_2$O, 99%), potassium iodide (KI, 99%), sodium hydrate (NaOH, 97%), sodium chloride (NaCl, 99.5%) were purchased from Sigma Aldrich and used as received; semiconductor quantum dots (SQDs, Qdot@800 ITK, Q21371MP) were purchased from Invitrogen Corporation; Bovine serum albumin (BSA, > 96%) and DNA polymerase (5U/uL) were purchased from Genview and Promega Corporations, respectivley. In all experiments, we used deionized water with a resistivity of 18.2 MΩ·cm, which was prepared by using a Millipore Mili-Q water system.

3.2 Synthesis of gold nanoparticles with different Shapes

Gold nanoparticles of four shapes, including spherical nanoparticles, triangular nanoplates, nanodiscs and nanorods were prepared using seed-mediated methods. These resulting Au nanoparticles were all stabilized with positively charged CTAB. Before experiments, all glasswares were washed with aquaregia (3:1 ratio by volume of HCl and HNO$_3$), and rinsed with deionized water several times.

Au triangular nanoplates were grown following a procedure modified from that reported by Millstone et al.[40,41] Specifically, the seeds were prepared by reducing HAuCl$_4$ (0.01 M, 1 mL) with a freshly prepared, ice-cold aqueous NaBH$_4$ (0.1 M, 1 mL) in fresh deionized water (36 mL), followed by rapid a stir mixing for 2 min. The resulting mixture was aged at room temperature (25 ^{0}C) for 4 hours to allow the hydrolysis of unreacted NaBH$_4$. Finally, the Au nanocrystal seeds were obtained with a plasmon resonance peak is at ca. 518 nm. After the aging period, five growth solutions (A, B, C, D and E) were prepared for the seed-mediated growth. The first two solutions (A and B) were identical, contained NaOH (0.1 M, 0.05 mL), ascorbic acid (0.1 M, 0.05 mL), KI (0.1 M, 4.5 μL), CTAB (0.05 M, 9.0 mL) and HAuCl$_4$ (10 mM, 0.25 mL). The other solutions C, D and E were identical, and contained NaOH (0.1 M, 0.25 mL), ascorbic acid (0.1 M, 0.25 mL), KI (0.1 M, 23 μL), CTAB (0.05 M, 45 mL) and HAuCl$_4$ (10 mM, 1.25 mL). Note that all these five groups of solutions were prepared by adding chemicals in the sequence listed above. Au triangular nanoplate growth was initiated by adding 1 mL of seed solution to solution A, which was gently shaken. 5 mL of growth solution A was then quickly added to B, followed by gentle shaking and 2, 4 and 6 mL of solution B were added to the solutions of C, D and E, respectively. After the addition, the colors of C, D and E changed from clear to deep magenta-purple over a period of 30 minutes for all preparations. Lastly, three Au TNPs samples with extinction maximum at ~1220, 1106 and 900 nm were obtained. Gold nanodiscs (Au NDs) were prepared based on the preparation of Au TNPs. When the growth of the Au triangular nanoplates (synthesized by using 4 mL seed solution) was conducted for 2 hours, the growth process was terminated by centrifugation and washing at 5000 rpm for 10 min for three times. Finally, all the precipitates were redispersed into 10 mL of deionized water, and then the solution was placed at 30 ^{0}C in a water bath for 12 h. Finally, the mixture of Au NDs and SNPs was obtained.

Au nanorods with large aspect ratio (15 ± 2) were grown according to a procedure modified from that reported by Duan *et al.*.[63] Specifically, Au seed solution was prepared by adding HAuCl$_4$ (0.5 mM, 5 mL) into CTAB solution (0.2 M, 5 mL) in a 25 mL beaker covered with a cling film. Then, a freshly prepared, ice-cold NaBH$_4$ solution (0.01 M, 0.6 mL) was added quickly to the mixture solution, followed by rapid stirring for 2 min. The seed solution was kept at 27 ^{0}C for 2 h before use. To grow Au NRs, HAuCl$_4$ (8 mM, 0.8 mL) was mixed with CTAB (0.067 M, 9 mL) in a 15 mL reagent bottle, followed by the addition of ascorbic acid (0.08 M, 0. 2 mL). After gently shaking, 20 μL of CTAB-stabilized Au seed solution was injected into the above growth solution. The solution was gently mixed for 1 min and left undisturbed overnight at 27 ^{0}C.

3.3 Shape and size separation of gold triangular nanoplates

Au TNPs synthesized using the method described as above usually contain nanoplates with various sizes and nanosphers. To obtain uniform Au TNPs, step separation of Au TNPs with different sizes from the impurity of nanosphers was employed. Specifically, a 45 mL mixture contained the as-prepared Au TNPs, SNPs and CTAB (0.05 M) was prepared in a cleaned beaker. NaCl solution (4.0 M, 0.2 mL) was added into the mixture, and the final mixed solution was left undisturbed for 4 h. Then, the supernatant solution was gently transferred to another cleaned beaker by a syringe. Au TNPs with larger surface areas were first adhered at the bottom of the beaker. After dropping 10 mL of CTAB (0.01 M) into the container and repeated pipetting with a straw, the first purified Au TNPs with larger surface areas were obtained. This is called the first step separation. In a similar way, the second step separation for purifying Au TNPs was initiated by adding 0.40 mL of NaCl (4.0 M) into the supernatant solution after the first separation. The supernatant was left undisturbed for 8 h, with the supernatant was thoroughly transferred to another cleaned beaker, the second purified Au TNPs with smaller surface areas were found adhered at the bottom. Nanoplate solution was obtained by adding 10 mL CTAB (0.01 M) to the beaker and repeated stirring. This is so-called the second separation. Similarly, the third and fourth step separations of Au TNPs with the smallest surface areas were performed with the successive addition of 0.6 and 0.4 mL of NaCl solution (4.0 M) into the supernatant solution and waiting for 12 and 14 h, respectively. Thus, by employing the different amount of Au nanoseeds in the growth of Au TNPs and using the particle's surface area-based shape and size separation, we can obtain purified Au TNPs with the edge length ranging from 40 to 180 nm.

3.4 Plasmon mode tuning of Au gold triangular nanoplates for fluorescence quenching of semiconductor quantum dots

Plasmon mode tuning of Au TNPs was carried out by using on-demand shape and size selecting. Purified Au TNPs with λ_{SPR} = 782, 805, 855, and 1060 nm were obtained based on the above-mentioned surface area-based purification method. 4 mL of each Au TNP solution ($\sim 3.0 \times 10^{-4}$ M) sample was centrifuged and washed with deionized water two times (the supernatant was thoroughly removed). Then, the purified Au TNPs with on-demand λ_{SPR} was added in 2.0 mL of SQDs solution (1 nM) and cultivated in dark place for 1h. After the SQDs were directly attached on the surface of the Au TNPs due to the electrostatic attraction between them, the fluorescence spectrum of the mixture contained Au TNPs and SQDs were measured.

3.5 Refractive index sensitivity measurement and proteins detection

Water-glycerol mixtures of varying volume ratios were used to change the refractive index of the surrounding medium of the purified Au TNPs. The volume percentages of glycerol in the liquid mixture were 0.66, 0.98, 1.46, 2.83, 3.99, 4.55, 5.62, 6.14, 7.14 and 9.00 %, and then the as-prepared purified Au TNPs were redispersed into the water-glycerol mixtures. Extinction spectra of the resulting dispersion solutions of Au TNPs were measured. The plasmon shift was plotted as a function of the refractive index, and the refractive index sensitivity was determined by linear fitting. In a similar manner, BSA and DNA polymerase detections were performed using the purified Au TNPs with SPRs

at 1217 and 1192 nm, respectively. Briefly, water-protein mixtures of varying volume ratios were used to protein detections based on the purified Au TNPs. For BSA detection, the volumes of BSA aqueous solution (0.2 mg/mL) of 1, 2, 3, 4, and 6 μL
5 were dispersed in water (2.0 mL), and then these water-protein mixtures were added into the as-prepared purified Au TNPs solution (0.5 mL), respectively. Similarly, 20, 46, 76, 106, and 156 μL DNA polymerase solution (0.05 U/μL) dispersed in water (2.0 mL) were also detected using the purified Au TNPs.3.6
10 Characterization of samples

3.6 Characterization of Samples

The scanning electron microscopy image was performed by using a Zeiss Auriga-39-34 SEM machine operated at an accelerating voltage of 5.0 kV. The transmission electron microscopy graph
15 was performed by using a JEOL 2010HT TEM machine operated at 100 kV. The extinction spectra were recorded on an ultraviolet-visible-near-infrared (UV-VIS-NIR) spectrophotometer (PerkinElmer Lambda 950). The reference we adopted was 3 mL deionized water. A Malvern Zetasizer NanoZS90 instrument was
20 employed to record the particle's Zeta potential and size distribution. The fluorescence spectra of the SQDs were measured using a spectrofluorometer (Fluoromax-4) with a slot width of 5 nm, and the excitation wavelength was set at 450 nm. The thickness of Au triangular nanoplate was measured by
25 atomic force microscopy (Nea SNOM, Nea Spec Company).

3.7 Computational simulations

The extinction spectra are calculated by the Finite Element Method with the help of the COMSOL software. We consider an x polarized plane wave normally incident on the Au triangular
30 nanoplate. The lengths of the regular triangle Au nanoplates are set to be 171, 144, and 120 nm, respectively. The thicknesses are 7 nm. The dielectric constant of Au is fitting the experimental data from Johnson and Christy with piecewise cubic interpolation.[64] The extinction spectrum is the sum of the
35 absorption and scattering spectrums which are calculated by the Poynting vector and scattering Poynting vector integrating on a close surface that enclose the Au triangular nanoplate, respectively. A Perfectly Matched Layers (PML) covers the simulated region to perform absorbing boundary.

40 ## 4 Conclusions

We have developed a facile surface area-based purification method to obtain homogenous nanostructures from the mixtures of nanoparticles prepared by chemical synthesis. Nanoparticles, including triangular nanoplates, nanodiscs, nanorods, and
45 spherical nanoparticles with almost the same mass and volume, can be easily separate from each other by this method, even when three of them are mixed together. By selecting Au triangular nanoplates with on-demand size, we can achieve purified Au TNPs with strong SPRs, locating from 766 to 1322 nm (within
50 the NIR optical window), and we successfully tune the plasmon modes of Au nanoplates into resonance with the emission of quantum dots, realizing the fluorescence resonance energy transfer which is useful for the purpose of biomedical applications and electronic devices. The as-prepared Au TNPs
55 can reach a purity of 98%, and present a RIS value as high as 963 nm/RIU, which closes to the limit of theoretical calculation. BSA and DNA polymerase concentration detection with the limits respectively up to 80 ppb and 1 U further demonstrate that our purified Au TNPs can be used to build a high sensitivity bio-
60 sensor. Since the surface area determines various important properties of nanostructures, such as the SPRs, light absorption and scattering coefficient of nanostructure in solar cell, as well as catalyst ability, a purification method directly based on surface area can greatly help to select nanomaterials with on demand size
65 and shape, which provide a new avenue for achieving homogenous nanostructures beneficial to the development of future functional nanodevices.

Notes and references

80 1. W. L. Barnes, A. Dereux and T. W. Ebbesen, *Nature*, 2003, **424**, 824–830.
2. E. Ozbay, *Science*, 2006, **311**, 189–193.
3. D. K. Gramotnev and S. I. Bozhevolnyi, *Nat. Photon.*, 2010, **4**, 83-91.
4 J. H. Hafner, C. L. Cheung and C. M. Lieber, *Nature*, 1999, **398**, 761–
85 762.
5 V. Amendola, S. Scaramuzza, S. Agnoli, S. Polizzi and Moreno eneghetti, *Nanoscale*, 2014, **6**, 1423–1433.
6 N. J. Halas, S. Lal, W. S. Chang, S. Link and P. Nordlander, *Chem. Rev.* 2011, **111**, 3913–3961.
90 7 X. P. Shen, T. J. Cui, D. Martin-Canob and F. J. Garcia-Vidalb, *Proc. Natl. Acad. Sci. USA*, 2013, **110**, 40–45..
8 E. Hutter and J. H. Fendler, *Adv. Mater.*, 2004, **16**, 1685–1706.
9 U. Fano, *Phys. Rev.,* 1961, **124**, 1866–1878.
10 B. Luk'yanchuk, N. I. Zheludev, S. A. Maier, N. J. Halas, P.
95 Nordlander, H. Giessen and C. T. Chong, *Nat. Mater.*, 2010, **9**, 707-715.
11 Z. K. Zhou, X. N. Peng, Z. J. Yang, Z. S. Zhang, M. Li, X. R. Su, Q. Zhang, X. Shan, Q. Q.Wang and Z. Zhang, Nano Lett., 2011, **11**, 49-55.
100 12 L. J. E. Anderson, C. M. Payne, Y. R. Zhen, P. Nordlander and J. H. Hafner, *Nano Lett*., 2011, **11**, 5034–5037.
13 J. Zhou, J. Zeng, J. Grant, H. Wu and Y. Xia, *Small,* 2011, **7**, 3308-3316.
14 M. Kim, N. Hohman, Y. Cao, K. N. Houk, H. Ma, A. K. Y. Jen and P.
105 S. Weiss, *Science*, 2011, **331**,1312-1315.
15 X. C. Ye, J. Chen, M. Engel, J. A. Millan, W. B. Li, L. Qi, G. Z. Xing, J. E. Collins, C.R. Kagan, J. Li, S. C. Glotzer and C. B. Murray, *Nat. Chem*., 2013, **5**, 466–473.
16 H. Zhang, M. Jin and Y. N. Xia, *Angew. Chem. Int. Ed*., 2012, **51**,
110 7656–7673.
17 E. Kazuma and T. Tatsuma, *Nanoscale*, 2014, **6**, 2397–2405.
18 C. M. Andolina, A. C. Dewar, A. M. Smith, L. E. Marbella, M. J. Hartmann and J. E. Millstone, *J. Am. Chem. Soc.*, 2013, **135**, 5266-5269.
115 19 H. Chen, X. Kou, Z. Yang, W. Ni and J. Wang, *Langmuir*., 2008, **24**, 5233–5237.
20 S. Lal, S. Link and N. J. Halas, *Nat. Photon*., 2007, **1**, 641-648.

21 C. Burda, X. Chen, R. Narayanan and M. A. El-Sayed, *Chem. Rev.*, 2005, **5**, 1025–1102.

22 M. L. Personick, M. R. Langille, J. Zhang, N. Harris, G. C. Schatz and C. A. Mirkin, *J. Am. Chem. Soc.*, 2011, **133**, 6170–6173.

23 F. Kim, S. Connor, H. Song, T. Kuykendall and P. Yang, *Angew. Chem.*, 2004, **116**, 3759–3763.

24 S. J. Hurst, E. K. Payne, L. D. Qin and C. A. Mirkin, *Angew. Chem. Int. Ed.*, 2006, **45**, 2672 –2692.

25 Z. K. Zhou, D. Y. Lei, J. M. Liu, X. Liu, J. C. Xue, Q. Z. Zhu, H. J. Chen, T. R. Liu, Y. Y. Li, H. B. Zhang and X. H. Wang, *Adv. Opt. Mater.*, 2014, **2**, 56–64.

26 H. Chen, L. Shao, Q. Li and J. Wang, *Chem. Soc. Rev.*, 2013, **42**, 2679–2724.

27 Q. Ruan, L. Shao, Y. Shu, J. Wang and H. Wu, *Adv. Opt. Mater.*, 2014, **2**, 64–73.

28 G. N. Meng, J. Paulose, D. R. Nelson and V. N. Manoharan, *Science*, 2014, **343**, 634–637.

29 D. A. Walker, E. K. Leitsch, R. J. Nap, I. Szleifer and B. A. Grzybowski1, *Nat. Nanotech.*, 2013, **8**, 676–681.

30 P. J. Straney, C. M. Andolina and J. E. Millstone, *Langmuir*, 2013, **29**, 4396–4403

31 K. C. Pradel, K. Sohn and J. X. Huang, *Angew. Chem. Int. Ed.* 2011, **50**, 3412–3416.

32 L. Bai, X. Ma, J. Liu, X. Sun, D. Zhao and D. G. Evans, *J. Am. Chem. Soc.*, 2010, **132**, 2333–2337.

33 O. Akbulut, C. R. Mace, R. V. Martinez, A. A. Kumar, Z. Nie, M. R. Patton and G. M. Whitesides, *Nano Lett.*, 2012, **12**, 4060–4064.

34 L. R. Huang, E. C. Cox, R. H. Austin and J. C. Sturm, *Science*, 2004, **304**, 987–990.

35 V. Sharma, K. Park and M. Srinivasarao, *Proc. Natl. Acad. Sci. USA*, 2009, **106**, 4981–4985.

36 N. Liu, M. L. Tang, M. Hentschel, H. Giessen and A. P. Alivisatios, *Nat. Mater.*, 2011, **10**, 631–636.

37 S. Kim, J. Jin, Y. J. Kim, I. Y. Park, Y. Kim and S. W. Kim, *Nature*, 2008, **453**, 757–760.

38 K. A. Homan, M. Souza, R. Truby, G. P. Luke, C. Green, E. Vreeland and S. Emelianov, *ACS Nano*, 2012, **6**, 641–650.

39 Z. X. Li, Y. Yu, Z. Y. Chen, T. R. Liu, Z. K. Zhou, J. B. Han, J. T. Li, C. J. Jin and X. H. Wang, *J. Phys. Chem. C*, 2013, **117**, 20127–20132.

40 J. E. Millstone, W. Wei, M. R. Jones, H. Yoo and C. A. Mirkin, *Nano Lett.*, 2008, **8**, 2656-2659.

41 J. E. Millstone, S. Park, K. L. Shuford, L. Qin, G. C. Schatz and C. A. Mirkin, *J. Am. Chem. Soc.*, 2005, **127**, 5312–5313.

42 S. R. Beeram and F. P. Zamborini, *ACS Nano*, 2010, **4**, 3633–3646.

43 K. Park, H. Koerner and R. A. Vaia, *Nano Lett.*, 2010, **10**, 1433–1439.

44 Y. J. Xiong, J. M. McLellan, J. Y. Chen, Y. D. Yin, Z. Y. Li and Y. N. Xia, *J. Am. Chem. Soc.*, 2005, **127**, 17118-17127.

45 M. R. Jones and C. A. Mirkin, *Angew. Chem. Int. Ed.*, 2013, **52**, 2886 –2891.

46 K. L. Young, M. R. Jones, J. Zhang, R. J. Macfarlane, R. Esquivel-Sirvent, R. J. Nap, J. Wu, G. C. Schatz, B. Lee and C. A. Mirkin, *Proc. Natl. Acad. Sci. USA*, 2012, **109,** 2240–2245.

47 R. Prasher, *Phys. Rev. Lett.*, 2005, **94**, 025901.

48 X. F. Yu, L. D. Chen, M. Li, M. Y. Xie, L. Zhou, Y. Li and Q. Q. Wang, *Adv. Mater.*, 2008, **20**, 4118–4123.

49 S. Kim, Y. T. Lim, E. G. Soltesz, A. M. De Grand, J. Lee, A. Nakayama, J. A. Parker, T. Mihaljevic, R. G. Laurence, D. M. Dor, L. H. Cohn, M. G. Bawedi and J. V. Frangioni, *Nat. Biotechnol.*, 2004, **22**, 93–97.

50 Y. Zhou, X. Zhou, D. J. Park, K. Torabi, K. A. Brown, M. R. Jones, C. Zhang, G. C. Schatz and C. A. Mirkin, *Nano Lett.*, 2014, **14**, 2157–2161.

51 R. Keunen, N. Cathcart and V. Kitaev, *Nanoscale*, 2014, **6**, 8045–8051.

52 P. Vasa, W. Wang, R. Pomraenke, M. Lammers, M. Maiuri, C. Manzoni, G. Cerullo and C. Lienau, *Nat. Photon.*, 2013, **7**, 128–132.

53 M. Barth, S. Schietinger, S. Fischer, J. Becker, N. Nüsse, T. Aichele, B. Löchel, C. Sönnichsen and O. Benson, *Nano Lett.*, 2010, **10**, 891–895.

54 M. Takase, H. Ajiki, Y. Mizumoto, K. Komeda, M. Nara, H. Nabika, S. Yasuda, H. Ishihara, and K. Marakoshi, *Nat. Photonic.*, 2013, **7**, 550–554.

55 D. Nepal, L. F. Drummy, S. Biswas, K. Park and R. A. Vaia, *ACS Nano*, 2013, **7**, 9064–9074.

56 L. Zhang, Y. Song, T. Fujita, Y. Zhang, M. Chen and T. H. Wang, *Adv. Mater.*, 2014, **26**, 1289-1294.

57 Y. Park, P. Taranekar, J. Y. Park, A. Baba, T. Fulghum, R. Ponnapati and R. C. Advincula, *Adv. Funct. Mater.*, 2008, **18**, 2071-2078.

58 B. Hötzer, I. L. Medintz and N. Hildebrandt, *Small*, 2012, **8**, 2297-2326.

59 A. V. Whitney, J. W. Elam, S. Zou, A. V. Zinovev, P. C. Stair, G. C. Schatz and R. P. Van Duyne, *J. Phys. Chem. B*, 2005, **109**, 20522–20528.

60 L. J. Sherry, R. Jin, C. A. Mirkin, G. C. Schatz and R. P. Van Duyne, *Nano Lett.*, 2006, **6**, 2060–2065.

61 J. Zhou, H. Yan, K. Ren, W. Dai and H. Wu, *Anal. Chem.*, 2009, **81**, 6627–6632.

62 S. S. Lange, K. Takata and R. Wood, *Nat. Rev. Cancer*, 2011, **11**, 96–110.

63 J. Duan, K. Park, R. I. MacCuspie, R. A. Vaia and R. Pachter, *J. Phys. Chem. C*, 2009, **113**, 15524–15532.

64 P. B. Johnson and R. W. Christy, *Phys. Rev. B*, 1972, **6**, 4370–4379.

Nanoscale Accepted Manuscript